Performance Enhancement of Parabolic Trough Collector by Using Homogenizer and Spiral

LI Peijing[1,2], LIU Taixiu[2,3], QIN Yuanlong[2,4], ZHENG Zhimei[2,5], ZHAO Kai[2,3], LIU Qibin[2,3*]

1. School of Energy, Power, and Mechanical Engineering, North China Electric Power University, Beijing 102206, China
2. Institute of Engineering Thermophysics, Chinese Academy of Sciences, Beijing 100190, China
3. University of Chinese Academy of Science, Beijing 100049, China
4. Department of Thermal Science and Energy Engineering, University of Science and Technology of China, Hefei 230027, China
5. Research Institute of Science and Technology of China Three Gorges Group Corporation, Beijing 100038, China

Abstract: In conventional parabolic trough collectors (PTCs), sunlight is concentrated at the bottom of the absorber tube, resulting in a significant circumferential temperature gradient across the absorber tube, heat loss and thermal deformation, which affects the safety and thermal performance of PTCs. In this study, a new receiver with homogenizer and spiral (RHS) is proposed, achieving the optical and thermal synergy to ameliorate the thermal deformation of the absorber tube and enhance thermal efficiency. A plane structure homogenizer is designed to improve uniformity of the concentrated solar flux of absorber tube through second reflection. In combination with the spiral, it improves the optical-thermal efficiency of the PTC by enhancing heat exchange between the fluid and the backlight side of the absorber tube. The performance of the collector is numerically studied by building a three-dimensional coupled light-thermal-structure model. The results show that the thermal deformation of the RHS is reduced by more than 96% and the optical-thermal efficiency is improved by 1.2%–0.63% compared with conventional receivers (CRs) under the same inlet temperature conditions. The proposed receiver is validated to be effective in reducing thermal deformation and improving optical-thermal efficiency.

1. Introduction

In order to deal with environmental and economic problems caused by the utilization of fossil fuels, and achieve global carbon dioxide reduction, the use of solar energy is a highly competitive approach [1]. Concentrated solar power (CSP) technologies [2, 3], including parabolic trough collector [4], linear Fresnel reflector [5], compound parabolic concentrator, etc, are attractive as the potential to produce continuous and large-scale electricity [6]. Among these technologies, parabolic trough collectors (PTCs) are more promising in the field of energy production [7].

A sketch of a conventional PTC is shown in Fig. 1, consisting of a receiver and a reflector. The receiver includes an absorber tube, with a working fluid as the

Nomenclature

A	aperture area of the reflector/m^2	w_1	width of homogenizer/m
c_p	specific heat/kJ·(kg·K)$^{-1}$	w	width of reflector/m
d_i	inner diameter of absorber tube/mm	Δy	thermal deformation
d_o	outer diameter of absorber tube/mm	**Greek symbol**	
F	focal length of reflector/m	α	open angle of homogenizer/(°)
H	pitch of spiral/mm	β	the angle of incidence/(°)
I_b	direct normal irradiance/W·m^{-2}	η_o	optical efficiency/%
l	length of reflector/m	η_T	thermal efficiency/%
l_1	length of homogenizer/mm	$\eta_{o\text{-}T}$	optical-thermal efficiency/%
l_2	installation height/mm	η_{ex}	exergy efficiency/%
l_3	the distance between the absorber and the focal point/mm	λ_c	thermal conductivity/W·(m·K)$^{-1}$
L_t	heat loss per unit length/W·m^{-1}	μ	dynamic viscosity/μPa·K
Pr_T	the turbulent Prandtl number	μ_t	turbulent dynamic viscosity/μPa·K
Q_a	solar energy absorbed by the absorber tube/W	ρ	density/kg·m^{-3}
Q_h	the heat carried away by working fluid/W	**Abbreviations**	
Q_{in}	irradiation hit the aperture of the reflector/W	CR	conventional receiver
S	heat source	DNI	direct normal irradiance
T_a	temperature of ambience/K	PTC	parabolic trough collector
T_{sun}	temperature of sun/K	RHS	receiver enhanced by homogenizer and spiral
t	thickness of spiral/mm		

heat carrier, a glass cover and a vacuum area between the two, as shown in Fig. 1(a). When the PTC is under solar radiation, the radiation reaching the receiver is first absorbed by the surface coating of the absorber tube, and the heat is transferred to the working fluid through convection heat transfer, as shown in Fig. 1(b).

Due to the limitation of line focusing, solar radiation reflected from the reflector is concentrated at the bottom (light-receiving side) of the absorber tube. Circumferential irradiation gradients lead to circumferential temperature gradients of the absorber tube, resulting in uneven thermal stress that further causes bending and deformation of the absorber tube and even damage to the external vacuum glass cover [8, 9]. Fig. 1(c) shows the deformation of the absorber tube in the working state. The data shows that 55% of PTC system failures are caused by broken glass and 29% detected vacuum failure [3]. Furthermore, excessive localized temperatures can cause selective coating failure and lead to oil penetration and pyrolysis, which limits the maximum operating temperature and increases heat loss.

Reducing the circumferential temperature gradient to alleviate the thermal deformation of the absorber tube is of great significance to improve the safety of PTC. The solutions can be approximately classified into two categories.

The first category of solutions is based on optical optimization methods: To homogenize the solar flux of absorber tube by changing the light distribution outside the receiver.

Amir et al. [10, 11] suggested rotating the receiver, and found that the maximum temperature of the absorber tube decreases only at a specific rotation frequency. Moreover, the increase of moving parts is not conducive to the long-term stable operation of PTCs. Yu et al. [12] designed two symmetrical solar mirrors to collect more solar light, which is influenced by the surface spectral emissivity. Gong et al. [13] and Spirke et al. [14] proposed the secondary reflector consisting of several parabolas with different focal lengths. An adaptive technique was used to optimize the shape and structure of the secondary reflector to absorb escaping sun rays, resulting in uniform solar flux and reduced optical loss [13]. Complex optimization process and high installation precision pose a challenge for the application of this method.

The secondary category of solutions is flow enhancement to enhance the convective heat transfer within the absorber tube. Two of the most common techniques are nanofluids and flow turbulators [15–18].

Nanofluids are used to increase the thermal conductivity of fluids by adding metal nanoparticles to

the base fluid. Bellos et al. [19], Javadi et al. [20] and Heyhat et al. [21] proved that the convection heat transfer of thermal oil is enhanced by adding nanoparticles through numerical and experimental investigations. However, some disadvantages of nanofluids, such as unstable condensation and high production cost, limit practical applications [22]. On the other hand, the use of flow turbulators has drawn increasing attention, and it has the same advantages as nanofluids. Mwesigye et al. [23] and Jaramilo et al. [24] investigated the performance of PTC with spiral insert. The results reveal that the temperature gradient of the absorber tube is minimized and thermal efficiency is increased under the action of the spiral. Many other tube inserts have also been extensively studied. Peng et al. [25, 26] recommended the ribs to enhance the convection heat transfer. Aggrey et al. [27] adopt perforated plate inserts for the heat transfer enhancement in the absorber tube. Javier et al. [28] enhanced the convection heat transfer by using internally finned tubes. Mehdi et al. [29] and Bohra et al. [30] carried out the thermal analysis of the receiver with metal foam. The simulation results show the circumferential temperature difference is reduced by more than 47% [30]. But, the flow resistance is dramatically increased compared with spirals.

There is a lot of interest in ameliorating the temperature gradient of the absorber tube. The optical optimization methods rely on high-precision component designs or materials. Since the backlit side of the absorber tube receives only a small amount of radiation, the use of flow turbulators in this part will not significantly improve heat transfer, which will cause an unnecessary pressure drop [31]. Few studies have combined optical enhancement methods and flow enhancement methods to achieve complementary advantages. In addition, there is a lack of in-depth research on the effect of temperature gradients on the structural stability of absorber tubes. It is necessary to focus on the thermal efficiency of the collector [32].

The present work designed a homogenizer with a biplane structure to homogenize the solar flux of the absorber tube. On this basis, a new receiver with a homogenizer and a spiral (RHS) is proposed, achieving the optical and thermal synergy. Spirals are commonly used as flow turbulators in conjunction with homogenizers to improve heat transfer on the backlit side of the absorber tube. The performances of the thermal, fluid and structure characteristics are numerically studied. The main contributions are summarized as:

(1) The homogenizer with a new structure is designed, and the new receiver with homogenizer and spiral (RHS) is proposed.

(2) A three-dimensional optical-thermal-structure model was developed to evaluate the performance of the

new receiver, and analyze the structural health of the absorber tube.

(3) The optical and thermal characteristics of the receiver and optical-thermal efficiency of PTC are numerically found. The influences of the key operating parameters on the performance of the system were investigated.

The rest of this paper is organized as follows. In Section 2, we described the new receiver with homogenizer and spiral, and presented its optimization process and design parameters. In Section 3, we developed an optical-thermal-structure couple model. In Section 4 we presented a comprehensive validation for the developed model. In Section 5, we investigated the optical, thermal, and structural properties and efficiency of the new receiver, and the effects of operating conditions are discussed. Finally, some crucial conclusions are given in Section 6.
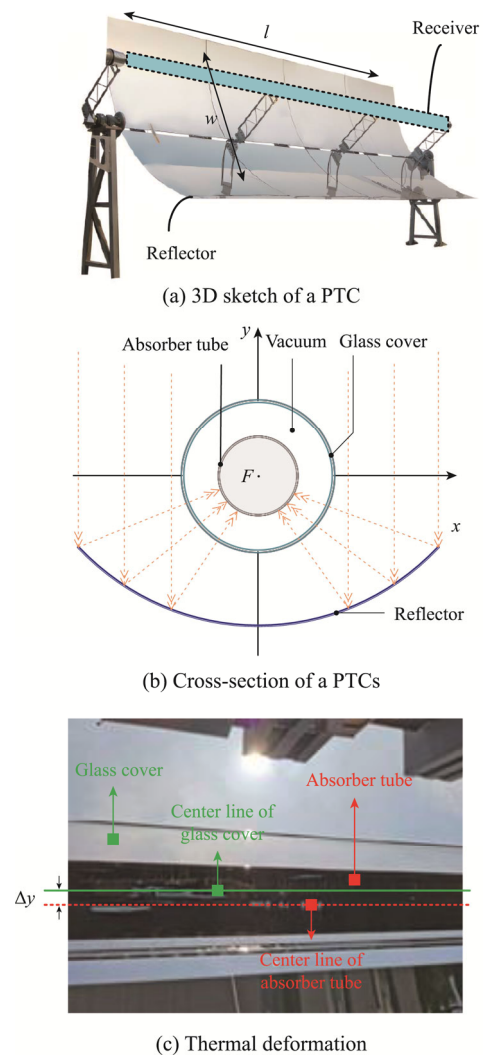

(a) 3D sketch of a PTC

(b) Cross-section of a PTCs

(c) Thermal deformation

Fig. 1   Sketch of conventional parabolic trough collectors

2. New Receiver

A typical commercial PTC of LS-2 was selected as the reference collector. The structure and schematic are shown in Fig. 1, and the parameters are presented in Table 1. The receiver is located at the focal point of the reflector, and there is little sunlight on the backlit side of the absorber tube due to the boundary angle.

To reduce the uneven circumferential temperature difference and increase the efficiency of the PTCs, in Fig. 2 a new receiver with a homogenizer and built-in spiral was proposed. The homogenizer can make the temperature uniform on the surface of the absorber tube, and the spiral changes the flow field of the working fluid. The homogenizer and spiral combination allows the working fluid to absorb heat evenly in the absorber tube.
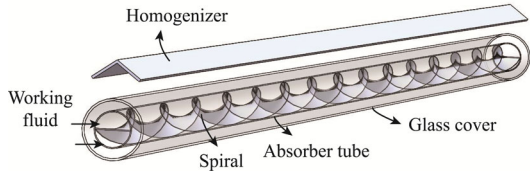

Fig. 2　New receiver with homogenizer and spiral

To alleviate uneven temperature distribution in the circumferential direction of the absorber tube, the design process of the homogenizer is as follows.

Firstly, to alleviate the uneven temperature distribution on the light-receiving and the backlit sides of the absorber tube, a homogenizer was installed on the top of the receiver to reflect the primary lights that escape the absorber tube to the backlit side of the receiver, as shown in Fig. 3. According to the principle of the parabolic mirror reflection, to make the primary light escape from the receiver, the receiver is installed away from the focus in the y-direction, and the boundary angle of the absorber tube (the angle between the primary reflected light tangents to the absorber tube) will change. In the new PTCs, the receiver position l_3 with the maximum boundary angle is chosen, as shown in Fig. 3(a).

In addition, the homogenizer is composed of two planes in an inverted v-structure, and the optical characteristics are the same as those of the reflector. To make the secondary light all reach the top of the absorber tube, the structural angel α satisfies:

$$180° - 2\beta < \alpha < 180° - \beta \qquad (1)$$

where β is the angle of incidence (the maximum angle between the primary ray reflected and the y-axis) is calculated by the focal length and width of the reflector:

$$\beta = \arctan\left(\frac{8wF}{16F^2 - w^2}\right) \qquad (2)$$

In order to reduce the shielding effect of the homogenizer on the optical efficiency and avoid the overflow of primary light, the width of the homogenizer w_1 satisfies:

$$w_1 \leq d_i \qquad (3)$$

To enhance the convective heat transfer within the absorber tube, a spiral that outer surface is tangent to the inner surface of the absorber tube was added to the absorber tube. The pitch H represents the distance that the working fluid rotates one revolution along with the flight, as shown in Fig. 3(b).

The pitch H of the spiral affects the pressure loss of the working fluid and the optical-thermal efficiency of PTCs. In this work, the spiral with H of 1040 mm is selected, and the influence of the pitch on the receiver performance is analyzed in Section 5.5.
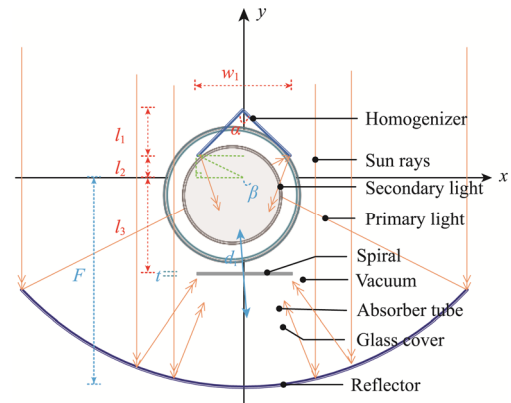
(a) *x-y* direction view
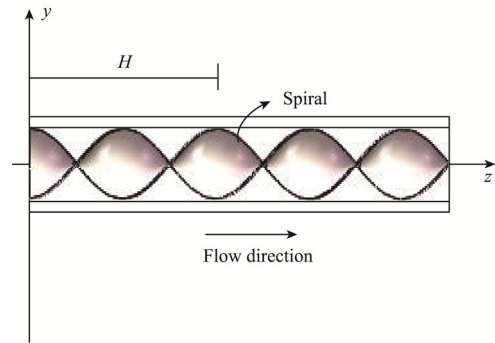
(b) *y-z* direction view

Fig. 3　New receiver

The parameters of the new receiver can be found in Table 1. The new structure has the following advantages:

(1) The homogenizer with the symmetrical inverted-v plane structure has a simple structure, few design parameters, and it is easy to install.

(2) The integral spiral increases the rigidity of the absorber tube.

(3) Spirals are used in conjunction with a homogenizer to enhance the heat transfer of the fluid on the backlist side.

In the trough receiver, Syltherm 800 oil was selected as a heat transfer fluid in the absorber tube, and the

thermophysical properties can be expressed as:

The density, ρ, of the heat transfer oil is calculated as [33]:

$$\rho = aT^2 + bT + c$$

where $a = -6.061\,657 \times 10^{-4}$,

$b = -4.153\,495 \times 10^{-1}$,   (4)

$c = 1.105\,702 \times 10^3$

where the suitable temperature range is 283.15–673.15 K.

The specific heat capacity, c_p, of the heat transfer oil can be predicted as [33]:

$$c_p = 0.001\,708T + 1.107\,798 \qquad (5)$$

where the suitable temperature range is 283.15–673.15 K.

The thermal conductivity, λ_c, of the heat transfer oil was calculated as [33]:

$$\lambda_c = aT^2 + bT + c$$

$a = -5.753\,496 \times 10^{-10}$

$b = -1.875\,266 \times 10^{-4}$ (6)

$c = 1.900\,210 \times 10^{-1}$

where the suitable temperature range is 283.15–673.15 K.

Table 1 Parameters of the conventional PTCs and the new receiver

	Parameters	Value
Reflector	Focal length, F/m	1.84
	Width, w/m	5
	Length, l/m	7.8
	Aperture area, A/m^2	39
	Solar reflectance	0.93
Absorber tube	Inner diameter, d/mm	66
	Outer diameter/mm	70
	Thermal conductance/W·(m·K)$^{-1}$	14.8+0.0153T
	Solar selective coating	$2 \times 10^{-7}T^{-2}$–1.0926 $\times 10^{-4}T$+0.076 922
Glass cover	Inner diameter/mm	0.112
	Outer diameter/mm	0.115
	Solar absorptance	0.02
	Transmissivity	0.95
	Thermal conductance/W·(m·K)$^{-1}$	1.20
New receiver	Distance from receiver to the focal point of reflector, l_3/mm	47
	Width of homogenizer, w_1/mm	66
	Length of homogenizer, l_1/mm	20.98
	Open-angle, α/(°)	113.5
	Installation height, l_2/mm	6.7
	Pitch of spiral, h	1040 mm
	Thickness of spiral, t	2 mm

The dynamic viscosity μ of the heat transfer oil can be predicted as [33]:

$$\mu = aT^4 + bT^3 + cT^2 + dT + e$$

$a = 6.672\,331 \times 10^{-7}$

$b = -1.566\,003 \times 10^{-3}$

$c = 1.388\,285$ (7)

$d = -5.541\,277 \times 10^2$

$e = 8.486\,612 \times 10^4$

where the suitable temperature range is 283.15–673.15 K.

3. Optical-Thermal-Structure Couple Model

The performance of PTCs was studied by developing an optical-thermal-structure coupled model. We provide an overview of the mathematical model in this section.

3.1 Optical part of the model

A three-dimensional optical model was established by the Monte Carlo ray-tracing method to simulate the transmission process of solar rays in the PTCs. The direct normal irradiance (DNI) is defined as 1000 W/m^2. The light emitted from the light source has a specific power. In the process of transmission, the solar light is absorbed by the solar coating after undergoing absorption, reflection and transmission of different surfaces, as well as the absorption and reflection in the glass cover. The light absorbed by the solar selective coating was recorded and the corresponding solar flux distribution was calculated [34–36]. Moreover, the non-parallel properties of the incident rays, the imperfect forms of the reflector and solar mirrors, and all relevant optical factors in Table 1 were taken into account. More details about this model can be found in Wang et al. [37].

3.2 Thermal part of the model

The heat transfer process: the radiation received by the receiver is first absorbed by the solar selective coating on the outer surface of the absorber tube, and then the absorbed power is transferred to the working fluid by the heat conduction between the walls of the absorber tube and the convective heat transfer between the inner wall of the absorber tube and the working fluid. Unabsorbed energy is transferred to the glass enclosure by radiative heat transfer, and then is lost to the environment by radiative heat transfer and convection heat transfer [38].

A three-dimensional steady-state model is established to analyze the heat transfer process. Each component of the receiver satisfies the energy conservation equation [39]:

$$\frac{\partial}{\partial x_i}\left(\lambda_c \frac{\partial T}{\partial x_i}\right) + S = 0 \qquad (8)$$

where λ_c is the thermal conduction, and S represents the heat source in the optical model [40].

In the fluid zone, the continuity equation, momentum equation and energy equation are satisfied [37].

$$\frac{\partial}{\partial x_i}(\rho u_i) = 0 \tag{9}$$

$$\frac{\partial}{\partial x_j}(\rho u_i u_j) = -\frac{\partial p}{\partial x_i} + \frac{\partial}{\partial x_j}\left[(\mu + \mu_t)\left(\frac{\partial u_i}{\partial x_j} + \frac{\partial u_j}{\partial x_i}\right)\right.$$
$$\left. -\frac{2}{3}(\mu + \mu_t)\frac{\partial u_i}{\partial x_i}\delta_{ij} - \frac{2}{3}\rho k \delta_{ij}\right] + F \tag{10}$$

$$\rho c_p u_i \frac{\partial T}{\partial x_i} = (k + k_T)\frac{\partial}{\partial x_i}\left(\frac{\partial T}{\partial x_i}\right) \tag{11}$$

where ρ is the density of working fluid; μ_t stands for the turbulent dynamic viscosity; c_p is the specific heat capacity; $k_T = c_p\mu_t/Pr_T$, where Pr_T denotes the turbulent Prandtl number.

The working fluid is turbulent in the absorber tube, and the standard k-ε model is shown in Eq. (12) and Eq. (13), where k represents the turbulent kinetic energy and ε represents the turbulent dissipation rate [12].

$$\frac{\partial(\rho u_i k)}{\partial x_i} = \frac{\partial}{\partial x_i}\left[\left(\mu + \frac{\mu_t}{\sigma_k}\right)\frac{\partial k}{\partial x_i}\right] + G_k - \rho\varepsilon \tag{12}$$

$$\frac{\partial(\rho u_i \varepsilon)}{\partial x_i} = \frac{\partial}{\partial x_i}\left[\left(\mu + \frac{\mu_t}{\sigma_\varepsilon}\right)\frac{\partial\varepsilon}{\partial x_i}\right] + c_1\frac{\varepsilon}{k}G_k - c_2\rho\frac{\varepsilon^2}{k} \tag{13}$$

where $C_k=0.09$, $c_1=1.44$, $c_2=1.92$, $\sigma_k=1.0$, $\sigma_\varepsilon=1.3$; G_k represents the production term and is calculated by Eq. (14).

$$G_k = \mu_t \frac{\partial u_i}{\partial x_j}\left(\frac{\partial u_i}{\partial x_j} + \frac{\partial u_j}{\partial x_i}\right) \tag{14}$$

The boundary conditions of the model are as follows:
(1) Inlet: $u_z=V_{in}$, $u_x = u_y =0$, $T=T_{in}$;
(2) Outlet: fully developed assumption [41]; The fully developed flow boundary condition prescribes that the tangential flow component on the boundary is zero;
(3) Ends of the receiver: adiabatic boundary;
(4) Absorber tube inner surface: no slip boundary.
The solid-fluid interfaces use logarithmic wall function boundary conditions. The logarithmic wall function used for the finite element method assumes that the flow is parallel to the wall at the beginning of the calculation domain, and the distance from the real wall is δ, and the velocity can be expressed as:

$$M^+ = \frac{M}{u_\tau} = \frac{1}{\kappa}\ln\left(\frac{\delta}{l^*}\right) + C^+, \mu_\tau = \sqrt{\frac{\tau_w}{\rho}},$$
$$l^* = \frac{\eta}{\rho\mu_\tau}, \delta_w^+ = \frac{\rho C_\mu^{1/4} k^{1/4}\delta}{\eta}, \delta_w^+ = \frac{\delta}{l^*}, C^+ = 5.5 \tag{15}$$

where M represents the velocity parallel to the wall, and κ is the Karman's constant, 0.42.

The radiation pattern on the outer surface of the glass tube is formed by surface-ambient radiation, and the effective sky temperature is 8 K lower than the ambient temperature [42]. The convective heat transfer coefficient between the glass cover and the environment is 10 W/m^2, and the ambient temperature, T_a is set to 298.15 K [34].

The governing equations are discretized by the finite elements method (FEM). The underlying finite element discretization method is the Galerkin method. Both the velocity components and the pressure field use the linear elements, and the linear system is solved by "PARDISO" in COMSOL Multiphysics.

3.3 Structure part of the model

In structural mechanics, the parameter changes in the material model are temperature-dependent, neglecting inertial forces.

The coupling of structural mechanics and heat transfer occurs on the absorber tube and the spirals made of 304 stainless steels, and the relevant parameters are shown in Table 2. The temperature serves as a heat carrier in the structural module, causing thermal strain.

The relationship between thermal strain and temperature expansion coefficient is as follows:

$$\varepsilon_{th} = \alpha(T - T_{ref}) \tag{16}$$

where ε_{th} represents the thermal strain; α is the thermal expansion coefficient, which is related to the material and temperature; $T_{ref}=298.15$ K represents the reference temperature.

The boundary conditions of the model are set as follow: the inlet end of the receiver is constrained to be fixed, and the outlet end is free to expand along the flow direction.

Table 2 Physical properties of TP304H steel [37]

Temperature/°C	20	100	200	300	400	500	600	700
Linear thermal expansion coefficient/10^{-6} °C^{-1}	–	17.1	17.4	17.8	18.3	18.8	19.1	19.4
Conductivity/W·(m·K)$^{-1}$	12.1	12.6	13.0	13.8	14.7	16.3	18.4	20.1
Elastic modulus/105 MPa	1.97	1.93	1.85	1.78	1.69	1.61	1.54	1.45
Density/kg·m^{-3}	7860							
Specific heat capacity/J·(kg·K)$^{-1}$	475							

3.4 Performance indexes

The following indexes are used to evaluate the performance of the new PTCs.

The optical efficiency, η_o of PTCs is the ratio of the solar energy absorbed by the absorber tube to the total solar radiant energy projected onto the aperture area of the reflector, and can be expressed as:

$$\eta_o = \frac{Q_a}{Q_{in}} = \frac{Q_a}{DNI \cdot A} \qquad (17)$$

$$Q_{in} = DNI \cdot A \qquad (18)$$

where Q_a represents the solar energy absorbed by the absorber tube; DNI is direct normal irradiance; A is the aperture area of the reflector.

The thermal efficiency, η_T of the PTCs is defined as the ratio of the heat carried away by the working fluid in the absorber tube to the solar energy absorbed by the absorber tube and can be calculated as:

$$\eta_T = \frac{Q_h}{Q_a} = \frac{\dot{m}\left(c_{p,out}\overline{T_o} - \overline{c_{p,in}T_i}\right)}{Q_a} \qquad (19)$$

$$Q_h = \dot{m}\left(c_{p,out}\overline{T_o} - \overline{c_{p,in}T_i}\right) \qquad (20)$$

where Q_h represents the heat absorbed by the working fluid; $\overline{T_o}$ and $\overline{T_i}$ represent the temperatures at the outlet and inlet ends of the working fluid, respectively.

The heat loss per unit length, L_t of the absorber tube is the ratio of the total heat loss of the absorber to the apparent length of the receiver, as shown in Eq. (21).

$$L_t = (Q_a - Q_h)/l \qquad (21)$$

The optical-thermal efficiency, $\eta_{o\text{-}T}$ of PTCs is defined as the ratio of the heat carried away by the working fluid in the absorber tube to the total solar radiant energy projected onto the aperture area of the collector:

$$\eta_{o\text{-}T} = Q_h/Q_{in} = \eta_o \cdot \eta_T \qquad (22)$$

The thermal-hydraulic efficiency, $\eta_{T\text{-}h}$ to evaluate the thermal hydraulic performance proposed by Kasperski [43]:

$$\eta_{T\text{-}h} = \frac{Q_h - W_p}{Q_{in}} = \frac{\dot{m}\left(c_{p,out}\overline{T_o} - c_{p,in}\overline{T_i}\right) - q_v\dfrac{\Delta p}{\eta_{blo}}}{DNI \cdot A} \qquad (23)$$

$$W_m = q_v\left(\Delta p/\eta_{blo}\right) \qquad (24)$$

where W_p is the pumping work to drive the working fluid flow; q_v is the volume flow rate of the working fluid; Δp is the pressure difference between the inlet pressure and outlet pressure of the working fluid; blower efficiency η_{blo} is assumed as 0.31 according to the blower characteristics in this paper [31].

The exergy efficiency, η_{ex} is expressed as the maximum work that can be produced by a collector, which is defined as the ratio of the exergy produced by the collector to the exergy flow of the solar flux:

$$\eta_{ex} = E_u/E_s \qquad (25)$$

where E_u for the collector equals to the Q_h minus the irreversibility as shown in Eq. (26) [44]. The exergy flow E_s of the solar radiation can be calculated by Eq. (27) [45]:

$$E_u = Q_h - \left[mc_pT_a\ln\left(\frac{\overline{T_o}}{\overline{T_i}}\right)\right] \qquad (26)$$

$$E_s = Q_{in} \cdot \left[1 - \frac{4}{3}\left(\frac{T_a}{T_{sun}}\right) + \frac{1}{3}\left(\frac{T_a}{T_{sun}}\right)^4\right] \qquad (27)$$

where T_{sun} represents the temperature of the sun, and is defined as 5770 K in our study [46].

4. Grid Independence Checking and Model Validation

To ensure the reliability of the model, grid independence checking and model validations are necessary [35, 47, 48]. Despite that the structure of the proposed receiver differs from conventional receiver, the heat transfer process is the same. The simulated data of conventional receiver is compared to the experimental data. If the simulated and experimental data agree well, the model can be considered reliable.

4.1 Grid independence checking

The vacuum cover uses the structured grid, and the fluid and metal part use the unstructured tetrahedral grid. The grid independence verification is shown in Fig. 4. When the number of grids increases from 1.08 million to 2.33 million, the changes in the maximum deformation and the average Nusselt number are almost negligible. Therefore, the grid with 1.08 million nodes is suitable in terms of accuracy and computational cost.
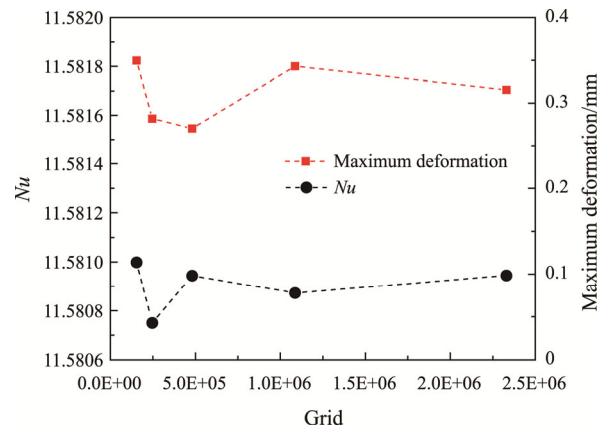

Fig. 4 Grid independence verification

4.2 Model validation

Fig. 5(a) shows the comparison of the optical simulation results and Jeter's result [49]. The data are

shown in close agreement, which proves the optical modelling in this paper is accurate and reliable.

In order to verify the reliability of the coupled model, the simulation results are compared with Sandia test [50] at the same operating conditions, as shown in Fig. 5(b). The relative errors of thermal efficiency between simulation results and the experimental results are within 4.46%, respectively, indicating that the proposed numerical model is feasible.
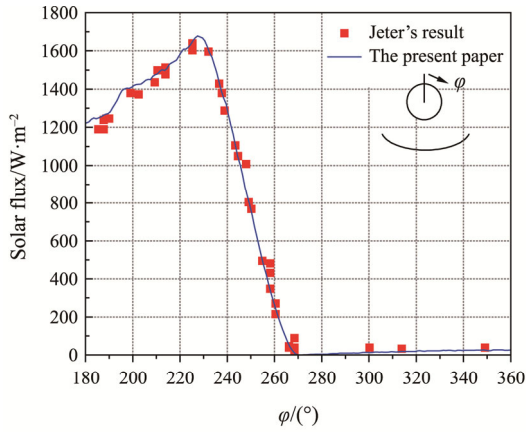
(a) Comparison of the solar flux
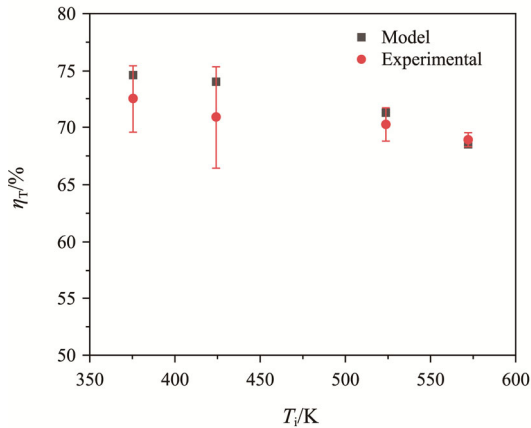
(b) Comparison of simulation and experimental results

Fig. 5   Model reliability verification

5. Result and Discussion

In this section, the optical, thermal, structural properties and efficiency of the proposed RHS were compared with conventional receivers (CRs) under different operating conditions, and the temperature distribution, the circumferential deformation and optical-thermal efficiency of the RHS are analyzed and discussed.

5.1 Optical performance

Fig. 6 presents the solar flux distribution of the absorber tube. Fig. 6(a) illustrates the overall solar flux

distribution of the new receiver. It can be seen that the solar flux is quite uniform, where the flux of the absorber tube is around 18 kW/m², and the distribution of solar flux along the receiver is consistent. The circumferential flux distribution of the cross-section of the absorber tube in different receivers is shown in Fig. 6(b). With $\varphi<90°$ and $\varphi>270°$, the flux on the backlit side of the RHS is significantly higher than that of the CRs due to the secondary reflection of the homogenizer. With $90°<\varphi<270°$, the flux on the light-receiving side of the RHS is lower than that of the CRs because the RHS is out of focus. The homogenizer reflects part of the light originally on the light-receiving side to the backlit side to reduce the unevenness in the circumferential direction. The results validate the superiority of the RHS.
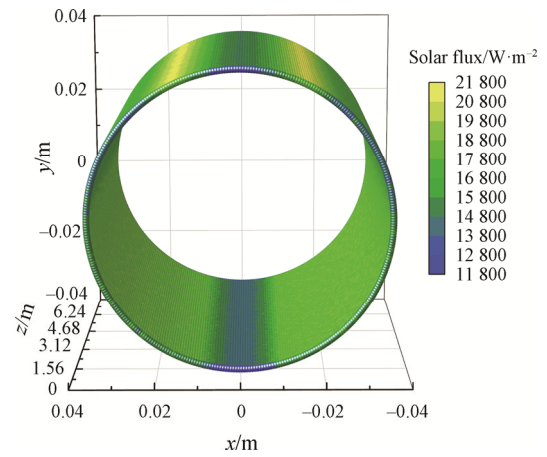
(a) The overall distribution of the RHS
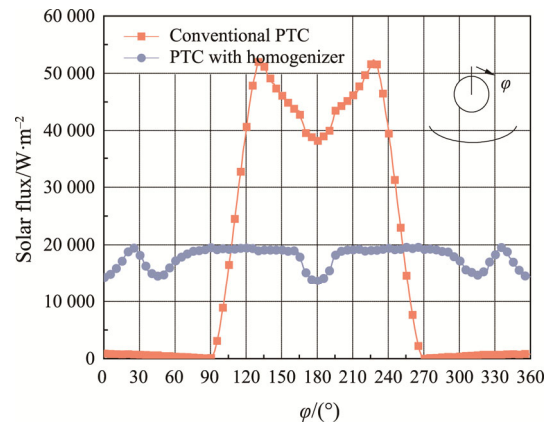
(b) Circumferential fluxes on absorber tubes

Fig. 6   Solar flux distribution

5.2 Thermodynamic properties of receivers

5.2.1 New receiver versus conventional receiver

(1) Temperature distribution of the absorber tube

Fig. 7 presents the temperature characteristics of the absorber tube on different receivers under typical

666

J. Therm. Sci., Vol.33, No.2, 2024

conditions (DNI is 1000 W/m^2; the inlet velocity of working fluid is 3 m/s and the inlet temperature is 573.15 K). The temperature distribution of the absorber tube on the RHS is shown in Fig. 7(a). We observe that the temperature at the outlet end of the absorber tube is higher than that at the inlet end, and the circumferential temperature difference increases slightly along the flow direction. This is because the solar heat of the fluid accumulates continuously along the direction of flow. Fig. 7(b) compares the circumferential temperature distribution of the absorber tube at z=7.8 m in different receivers. It can be found that the circumferential temperature difference in the RSH decreases compared with the CRs because the maximum temperature of the absorber tube decreases and the minimum temperature increases. This is because the solar flux distribution in the circumferential direction of the absorber tube in the RHS is uniform, and the absorber tube is uniformly heated.
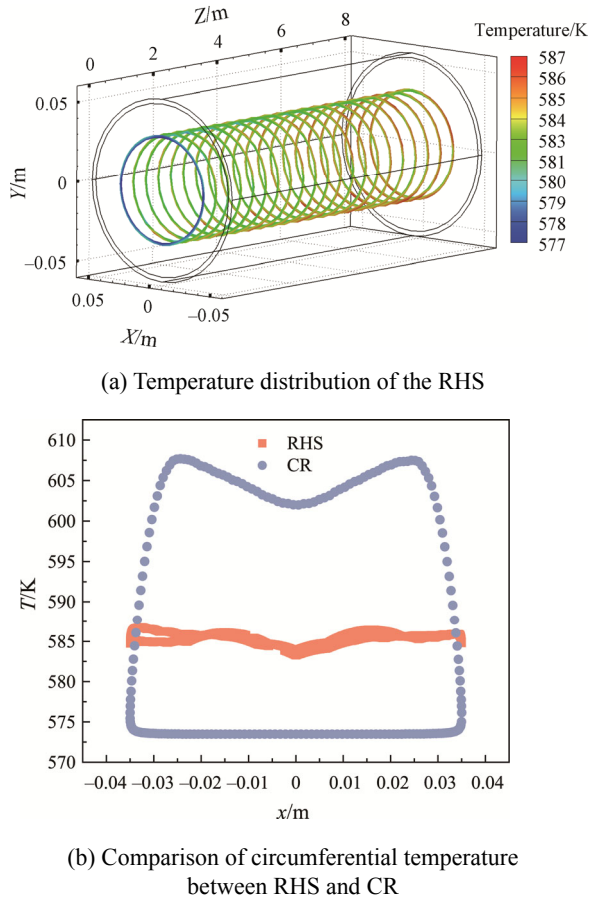

(a) Temperature distribution of the RHS

(b) Comparison of circumferential temperature between RHS and CR

Fig. 7 Temperature distribution

(2) Heat transfer of working fluid

Fig. 8 shows the cross-section temperature distribution of the working fluid in different receivers under typical conditions (DNI is 1000 W/m^2; the inlet velocity of working fluid is 3 m/s and temperature is 573.15 K). It

can be found that the average temperature of the working fluid increases along the flow direction because the working fluid continues to absorb heat. In the same section, the temperature near the wall is higher than the center of the RHS. There is a significant temperature gradient between the light-receiving side temperature and the backlit side of the working fluid in the CRs. On the one hand, the working fluid in the RHS is heated uniformly due to the uniform circumferential temperature distribution of the absorber. On the other hand, the spiral changes the flow of the fluid and enhances the internal heat transfer.
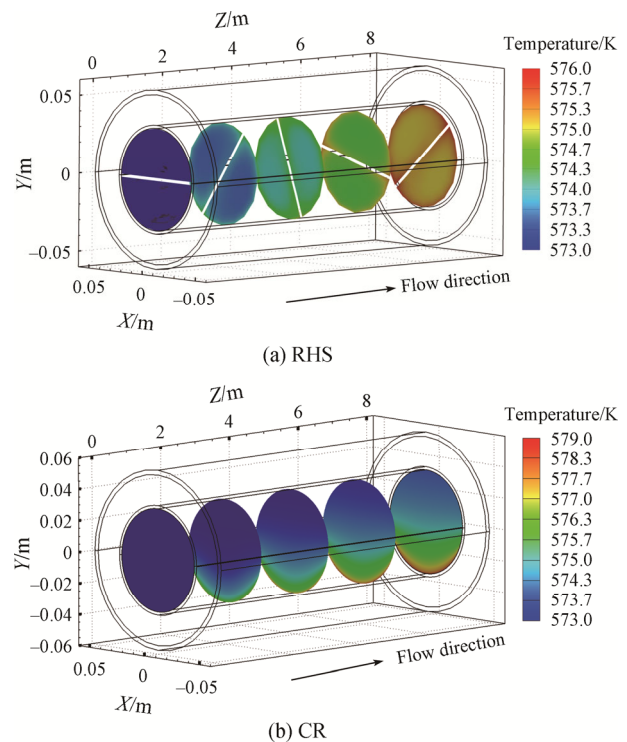

(a) RHS

(b) CR

Fig. 8 Temperature distribution of working fluid in different receiver

(3) Flow characteristics of velocity

Fig. 9 shows the velocity distribution of the fluid at the outlet of different receivers when the inlet velocity is 3 m/s. It can be found that the fluid velocity tends to decrease outward from the center due to the presence of the boundary layer. Compared with the CR, the center velocity of the fluid in the RHS increases by 11%, and the distance from the boundary decreases, indicating better mixing of the working fluid in the RHS. As a result, the heat transfer between the fluid and the boundary in the RHS is enhanced due to the increase in the heat transfer coefficient.

5.2.2 Temperature difference characteristics

Fig. 10 compares the circumferential temperature difference of the absorber tube on the RHS and the CR

under the typical ranges of the DNI, inlet velocity and inlet temperature of the working fluid.

(1) Influence of the DNI

Fig. 10(a) shows the circumferential temperature difference of the absorber tube on different receivers under different DNIs when the inlet velocity and temperature are 3 m/s and 573.15 K, respectively. It can be found that the circumferential temperature difference of the absorber tube increases with DNIs. When the DNI increases from 200 W/m^2 to 1000 W/m^2, the circumferential temperature difference of the absorber tube in the RHS increases from 0.85 K to 5.5 K. The temperature difference is caused by the uneven heat flux in the circumferential direction of the absorber tube. As the DNI increases, the inhomogeneity of temperature increases, and this phenomenon is more obvious in the CR. This is because the light-receiving side absorbs more
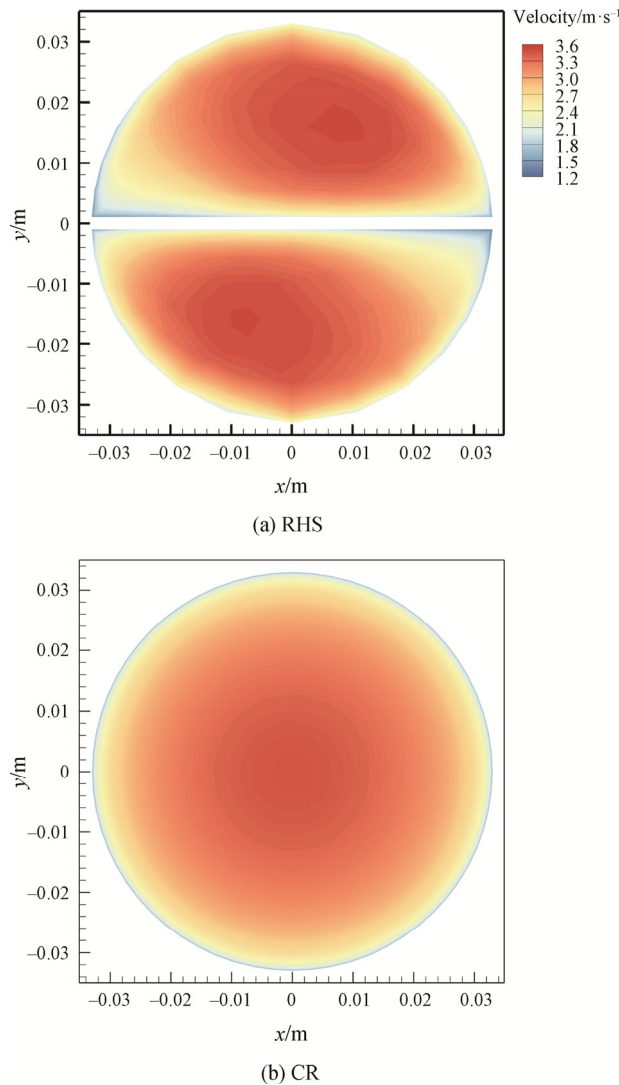
solar heat in the CR. In addition, compared with the CR, the circumferential temperature difference of the absorber tube in the RHS is reduced by 6.9 K to 34 K, with an improvement of 87.6%–83.8%, when the DNI is increased from 200 W/m^2 to 1000 W/m^2.

(2) Impact of inlet velocity of the working fluid

Fig. 10(b) shows the circumferential temperature difference of the absorber tube on different receivers
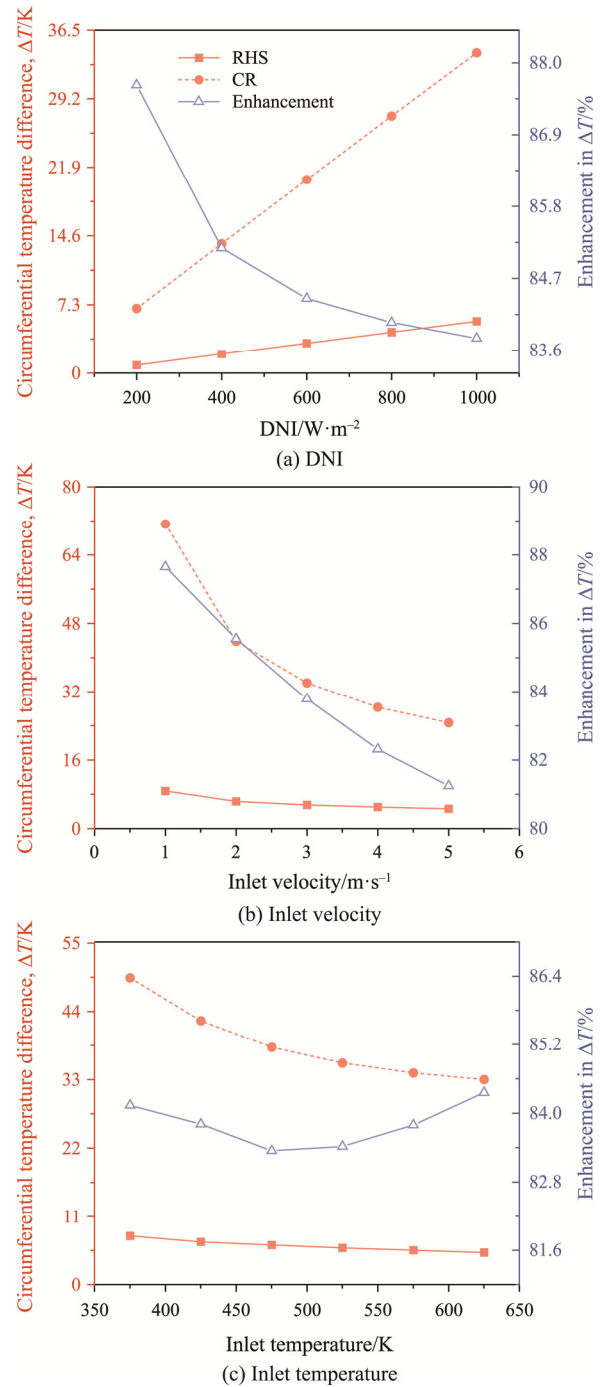

(a) RHS

(b) CR

Fig. 9   Velocity distribution of working fluid in the different receiver

(a) DNI

(b) Inlet velocity

(c) Inlet temperature

Fig. 10   Circumferential temperature difference of absorber tube comparison between the CR and RHS under different boundary conditions

under different inlet velocities of the working fluid when the DNI is 1000 W/m^2 and the inlet temperature is 573.15 K. It can be found that the circumferential temperature difference of the absorber tube decreases with the increase of velocity. When the velocity increases from 1 m/s to 5 m/s, the circumferential temperature difference of the absorber tube in RHS decreases from 8.8 K to 4.6 K. This is because the heat absorption of the working fluid increases with velocity. Hence, the temperature of the absorber tube decreases, and the circumferential temperature difference is weakened. In addition, compared with the CR, the circumferential temperature difference of the absorber tube in the RHS is reduced by 62.5 K to 20.1 K, with an improvement of 87.7%–81.2%, when the inlet velocity changes from 1 m/s to 5 m/s.

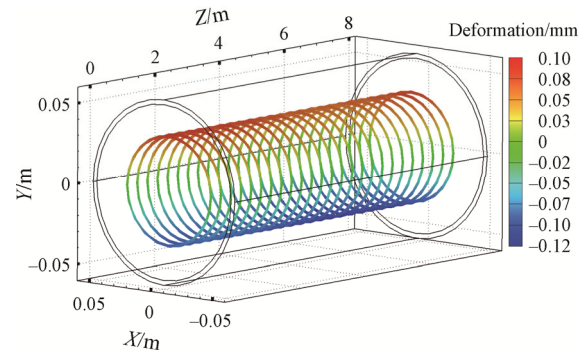(3) Influence of inlet temperature of working fluid

Fig. 10(c) shows the circumferential temperature difference of the absorber tube on different receivers under different inlet temperatures of working fluid when the DNI is 1000 W/m^2 and the inlet velocity is 3 m/s. It can be found that the circumferential temperature difference of the absorber tube decreases with the increase in temperature. When the temperature increases from 373.15 K to 623.15 K, the circumferential temperature difference of the absorber tube in the RHS changes from 7.8 K to 5.2 K. The reason is that as the fluid temperature rises, the Reynolds number rises as well, and the heat exchange between the fluid and the absorber tube increases, and the circumferential temperature difference is weakened. In addition, compared with the CR, the circumferential temperature difference of the absorber tube in the RHS is reduced by 49.4 K to 33.0 K when the inlet temperature changes from 373.15 K to 623.15 K.

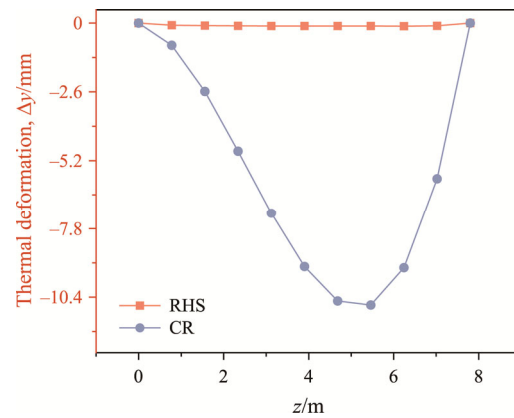## 5.3 Thermal deformation of the absorber tube

5.3.1 New receiver versus conventional receiver

Fig. 11 presents the thermal deformation of the absorber tube on different receivers when the DNI is 1000 W/m^2, and the inlet velocity of working fluid is 3 m/s and the inlet temperature is 573.15 K. The thermal deformation of the absorber tube in the RHS is shown in Fig. 11(a), and it can be found that the circumferential deformation of the absorber tube is almost unchanged along the flow direction, which is within 0.12 mm. The reason is that the circumferential deformation is caused by the uneven circumferential temperature distribution of the absorber tube, and the circumferential temperature difference of the absorber tube in the RHS is quite small.

Fig. 11(b) compares the thermal circumferential deformation of the absorber tube along the flow direction in different receivers. It can be found that the thermal deformation at both ends of the absorber tube in the CR is small, and larger along the flow direction due to

(a) Thermal deformation of the RHS

(b) Comparison of thermal deformation between RHS and CR

Fig. 11   Thermal deformation

mechanical constraints. Compared with the CR, the thermal deformation of the absorber tube in the RHS is almost zero due to the elimination of the circumferential temperature difference.

5.3.2 Thermal deformation characteristics

Fig. 12 compares the circumferential temperature difference of the absorber tube in the RHS and the CR under different DNIs, inlet velocities and inlet temperatures of working fluid.

Fig. 12(a) shows the thermal deformation of the absorber tube in different receivers when the inlet velocity of the working fluid is 3 m/s; the inlet temperature is 573.15 K, and the DNI varies from 200 W/m^2 to 1000 W/m^2. It can be found that the thermal deformation of the absorber tube increases with the increase of DNIs, which is consistent with the variation of the circumferential temperature difference. When the DNI increases from 200 W/m^2 to 1000 W/m^2, the thermal deformation of the absorber tube in the RHS is increased from 0.09 mm to 0.12 mm, and the thermal deformation is improved by 96.0%–98.8% compared with the absorber tube in the CR.

Similarly, the variation law of the circumferential temperature difference with the inlet velocity of the

working fluid is consistent with the circumferential temperature difference of the absorber tube, as shown in Fig. 12(b). When the DNI is 1000 W/m², the inlet temperature of the working fluid is 573.15 K, and the inlet velocity is increased from 1 m/s to 5 m/s, and the circumferential deformation of the absorber tube in the RHS is 0.17–0.11 mm, which is an improvement of 98.30%–98.51% compared with the CR.

Fig. 12(c) shows the thermal deformation of the absorber tube in different receivers when the DNI is 1000 W/m² and the inlet velocity is 3 m/s, and the inlet temperature varies from 373.15 K to 623.15 K. It can be observed that the thermal deformation of the absorber tube in the RHS decreases with the increase of the inlet temperature, which is the opposite of that in the CR. This is because the circumferential temperature difference of the absorber tube in the RHS is very small, and the thermal deformation is mainly caused by thermal strain due to temperature difference. In addition, when the inlet temperature is increased from 373.15 K to 623.15 K, the thermal deformation of the absorber tube in the RHS is increased from 0.09 mm to 0.14 mm, and the thermal deformation is improved by 99.4%–98.7% compared with the absorber tube in the CR.

5.4 Efficiency and loss analysis

5.4.1 Optical efficiency and thermal efficiency

Fig. 13(a) shows the optical losses and the optical efficiencies of the PTCs with different receivers when DNI is 1000 W/m². The optical efficiency of the RHS is 78.75%, which is 1.16% lower than that of the CR. The main reasons are summarized as follows. (1) The optical
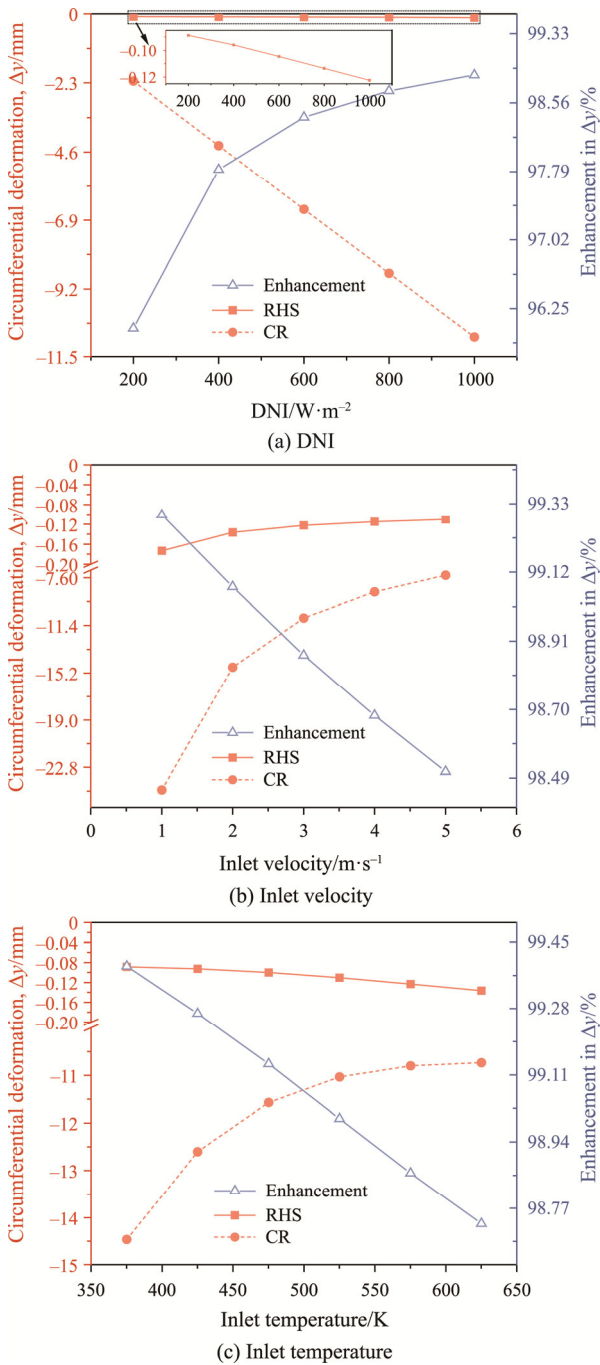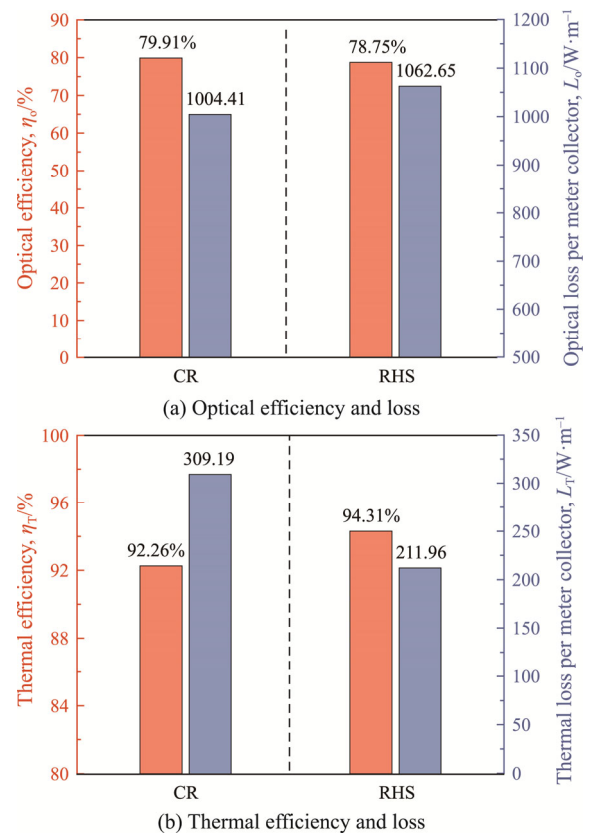

(a) DNI

(b) Inlet velocity

(c) Inlet temperature

Fig. 12   Circumferential deformation of absorber tube comparison between the CR and RHS under different boundary conditions

(a) Optical efficiency and loss

(b) Thermal efficiency and loss

Fig. 13   Optical efficiency and thermal efficiency of the PTCs in the CR and RHS

670

J. Therm. Sci., Vol.33, No.2, 2024

loss of the RHS is increased by 58.24 W/m compared to the CR; (2) The light radiation is absorbed multiple times to produce losses.

Although the optical efficiency is sacrificed, the thermal efficiency of PTCs with the RHS is improved. Fig. 13(b) presents the thermal efficiencies and thermal losses of PTCs with different receivers when DNI is 1000 W/m^2; inlet velocity of working fluid is 3 m/s, and inlet temperature is 573.15 K. The thermal efficiency of the RHS is 94.31%, which is 2.22% higher than that of the CR. The reason is that the maximum temperature of the absorber tube in the RHS is reduced, and the heat loss is reduced by 97.23 W/m compared with the CR.

5.4.2 Optical-thermal efficiency

Considering η_o and η_T in Fig. 13, the optical-thermal efficiency of PTCs with the CR and the RHS can be obtained in Fig. 14. It can be observed that with the increase in the inlet temperature, the optical-thermal efficiency $\eta_{o\text{-}T}$ of PTCs decreases. The reason is that the heat dissipation loss from the absorber tube to the environment increases as the temperature increases. The RHS achieves a higher $\eta_{o\text{-}T}$ than the CR. It can be found from the right coordinate axis that $\eta_{o\text{-}T}$ of the RHS is 1.2%–0.63% higher than that of the CR when the inlet temperature is 373.15 K–623.15 K. Combining with the temperature difference distribution in Fig. 8, the improvement in the temperature difference by the RHS weakens with the increase of temperature, and the enhancement of $\eta_{o\text{-}T}$ decreases slightly.

5.4.3 Exergy performance

Fig. 15 shows the exergy efficiency of the CR and the RHS under different inlet temperatures of the working fluid. The exergy efficiencies of different receivers show similar trends. With the increase of the inlet temperature, the exergy efficiency increases in the temperature range
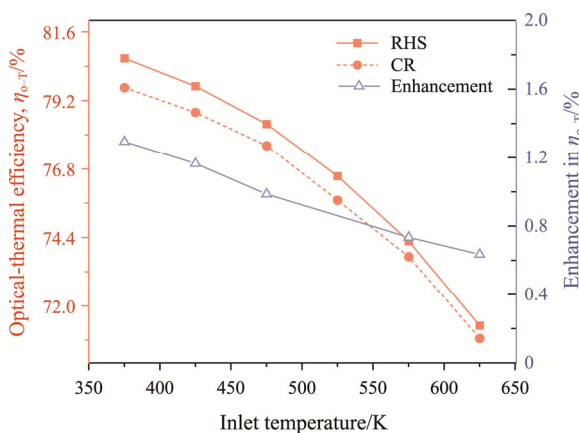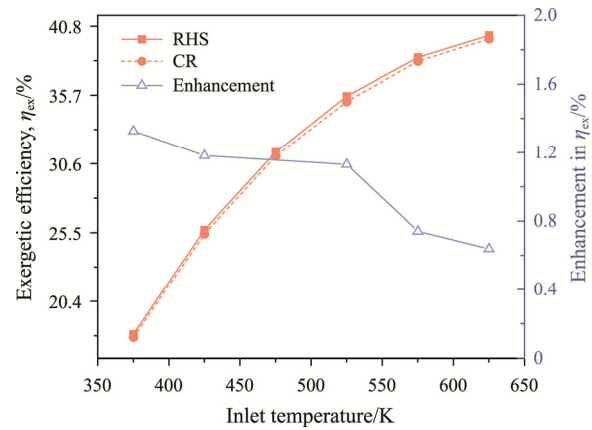

Fig. 15 Energy efficiency comparison of PTCs with CR and RHS when DNI is 1000 W/m^2

of 373.15 K–623.15 K. This is because both thermal energy transfer to the fluid and irreversible losses decrease with increasing temperature. The RHS achieves higher exergy efficiency than the CR. From the right coordinate axis, it can be found that when the inlet temperature is 373.15 K–623.15 K, the exergy efficiency of the RHS is 1.32%–0.63% higher than that of the CR.

5.4.4 Thermal-hydraulic efficiency

Fig. 16(a) shows the relationship between the thermal-hydraulic efficiency and the inlet velocity of the working fluid at different pitches when the DNI is 1000 W/m^2, and the inlet temperature is 573.15 K. As the inlet velocity of working fluid increases, the thermal-hydraulic efficiency shows a pattern of first increasing and then decreasing. When the inlet velocity is less than 2 m/s, as the velocity increases, the thermal-hydraulic efficiency increases, and the thermal-hydraulic efficiency of RHS is greater than that of the CR. At this time, the smaller the pitch, the greater the thermal-hydraulic efficiency. When the inlet velocity is greater than 2 m/s, as the inlet velocity increases, the thermal-hydraulic efficiency decreases, and the RHS of the thermal-hydraulic efficiency decreases faster than that of the CR. At this time, the smaller the pitch, the smaller the thermal-hydraulic efficiency.

Fig. 16(b) shows the relationship between the optical-thermal efficiency and the thermal-hydraulic efficiency of different pitches in RHS and CR when the DNI is 1000 W/m^2, and the inlet velocity of working fluid is 3 m/s and the inlet temperature is 573.15 K. It can be found that the optical-thermal efficiency is inversely proportional to the thermal-hydraulic efficiency in the RHS. The optical-thermal efficiency of RHS is greater than that of CR, and the optical-thermal efficiency increases as the pitch decreases. The thermal-hydraulic efficiency of RHS first increases and then slightly
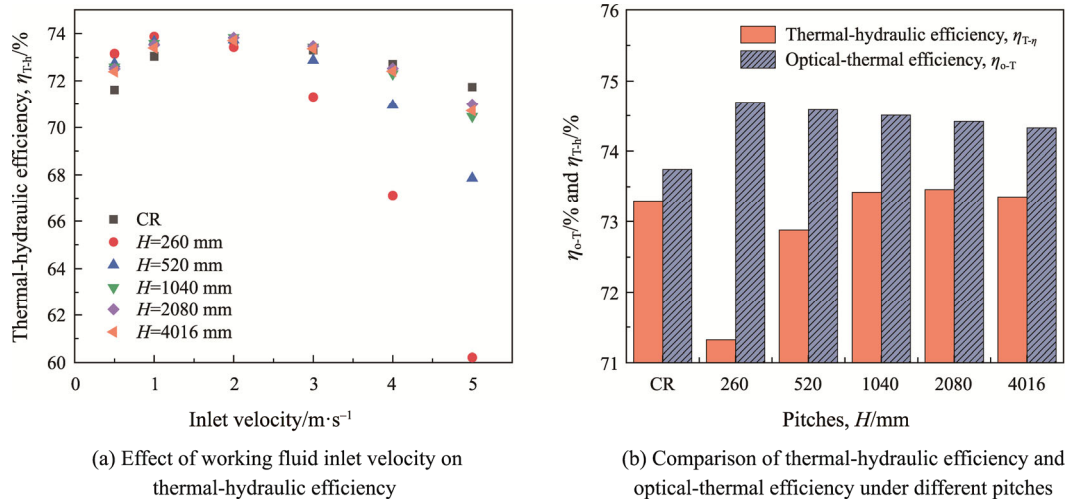

Fig. 14 Optical-thermal efficiency comparison of PTCs with CR and RHS when the DNI is 1000 W/m^2

(a) Effect of working fluid inlet velocity on thermal-hydraulic efficiency

(b) Comparison of thermal-hydraulic efficiency and optical-thermal efficiency under different pitches

Fig. 16 Effect of working fluid inlet velocity and pitches on thermal-hydraulic efficiency and the comparison between thermal-hydraulic efficiency and optical-thermal efficiency

decreases with the increase of pitch. When the pitch is less than 520 mm, the thermal-hydraulic efficiency of RHS is significantly lower than that of CR, and when the pitch is greater than 1040 mm, the thermal-hydraulic efficiency of RHS is higher than that of CR. This is because a smaller pitch increases the heat and mass transfer between the working fluid and the absorber wall, leading to an increase in optical-thermal efficiency. However, a smaller pitch also results in a higher inlet-outlet pressure difference for the working fluid, which reduces the thermal-hydraulic efficiency. Taking into account both the optical-thermal efficiency and thermal-hydraulic efficiency, the RHS with a pitch of 1040 mm is the optimal choice, which increases the optical-thermal efficiency by 1% and the thermal-hydraulic efficiency by 0.2% compared to the CR.

5.5 General comparison

Table 3 compares the thermal deformation, the optical-thermal efficiency, and the thermal-hydraulic efficiency between RHS and receivers with only homogenizers or spiral when the DNI is 1000 W/m², and the inlet velocity of working fluid is 3 m/s and the inlet temperature is 573.15 K. The RHS has advantages in thermal deformation. The receiver with only spiral has the highest optical-thermal efficiency and the thermal-hydraulic efficiency, but no significant improvement in thermal deformation. The receiver with only spiral has the lowest optical-thermal efficiency and the thermal-hydraulic efficiency, and there is a significant improvement in thermal deformation. Considering both thermal deformation and efficiency, RHS is the most advantageous.

Table 3 Comparison between RHS, receiver with only homogenizer and receiver with only spiral and conventional receiver

Performance indexes	The RHS	Receiver with spiral only
The thermal deformation, Δy/mm	0.09	8.38
The optical-thermal efficiency, η_{o-T}/%	74.51	77.91
The thermal-hydraulic efficiency, η_{T-h}/%	73.42	76.81

Performance indexes	Receiver with homogenizer only	Conventional receiver
The thermal deformation, Δy/mm	0.13	10.4
The optical-thermal efficiency, η_{o-T}/%	72.32	73.74
The thermal-hydraulic efficiency, η_{T-h}/%	71.87	73.30

6. Conclusions

To alleviate the thermal deformation and increase the optical-thermal efficiency of PTCs, a new receiver with homogenizer and spiral (RHS) is proposed. The optical performances were tested under DNIs varying from 200 W/m² up to 1000 W/m². Despite a slight reduction in optical losses, the new receiver has a uniform distribution of solar flux, which reduces heat losses and improves the thermal efficiency under different operating conditions. An optical-thermal-structure model is developed to analyze the thermal characteristics and efficiency performance of the RHS. The following conclusions are obtained.

(1) The circumferential temperature difference of the RHS under all inlet conditions (with the DNI of

200–1000 W/m^2, the inlet velocity of 1–5 m/s, and the inlet temperature of 373.15 K–623.15 K) is reduced by 5.2 K–62.5 K compared with CRs. The circumferential deformation difference of the RHS is reduced by 96%–99.4% under all the conditions.

(2) The flow center is dispersed to the boundary by spiral and the center velocity is increased by 11%. Under the action of the homogenizer, the fluid can evenly absorb heat on the tube wall while strengthening fluid mixing, which can effectively reduce the heat loss and improving thermal efficiency of PTC.

(3) Performance evaluation under the DNI (1000 W/m^2) and inlet velocity (3 m/s) and inlet temperature (573.15 K) indicates that the RHS can reduce the heat loss of the absorber by 97.23 W/m and improve the optical-thermal efficiency by 1.2%–0.63% compared with CRs under the same inlet temperature conditions.

(4) The RHS with a pitch of 1040 mm is the optimal choice, which increases the optical-thermal efficiency by 1% and the thermal-hydraulic efficiency by 0.2% compared to the CR.

Acknowledgements

Conflict of Interest

LIU Qibin is an editorial board member for Journal of Thermal Science and was not involved in the editorial review or the decision to publish this article. All authors declare that there are no competing interests.

References

[1] He Y.L., Wang K., Qiu Y., Du B.C., Liang Q., Du S., Review of the solar flux distribution in concentrated solar power: Non-uniform features, challenges, and solutions. Applied Thermal Engineering, 2019, 149: 448–474.

[2] Wang J., Qiu Y., Li Q., Xu M., Wei X., Design and experimental study of a 30 kWe adjustable solar simulator delivering high and uniform flux. Applied Thermal Engineering, 2021, 195: 117215.

[3] Sun J., Zhang Z., Wang L., Zhang Z., Wei J., Comprehensive review of line-focus concentrating solar thermal technologies: Parabolic Trough Collector (PTC) vs Linear Fresnel Reflector (LFR). Journal of Thermal Science, 2020, 29: 1097–1124.

[4] Fan M., Liang H., You S., Zhang H., Yin B., Wu X., Applicability analysis of the solar heating system with parabolic trough solar collectors in different regions of China. Applied Energy, 2018, 221: 100–111.

[5] Qiu Y., He Y.L., Cheng Z.D., Wang K., Study on optical and thermal performance of a linear Fresnel solar reflector using molten salt as HTF with MCRT and FVM methods. Applied Energy, 2015, 146: 162–173.

[6] Mehos M., Turchi C., Vidal J., Wagner M., Ma Z., Ho C., Kolb W., Andraka C., Kruizenga A., Concentrating solar power Gen3 demonstration roadmap, in, National Renewable Energy Lab.(NREL), Golden, CO (United States), 2017.

[7] Bellos E., Tzivanidis C., Alternative designs of parabolic trough solar collectors. Progress in Energy and Combustion Science, 2019, 71: 81–117.

[8] Sandeep H.M., Arunachala U.C., Solar parabolic trough collectors: A review on heat transfer augmentation techniques. Renewable and Sustainable Energy Reviews, 2017, 69: 1218–1231.

[9] Li L., Sun J., Li Y., Thermal load and bending analysis of heat collection element of direct-steam-generation parabolic-trough solar power plant. Applied Thermal Engineering, 2017, 127: 1530–1542.

[10] Norouzi A.M., Siavashi M., Khaliji Oskouei M., Efficiency enhancement of the parabolic trough solar collector using the rotating absorber tube and nanoparticles. Renewable Energy, 2020, 145: 569–584.

[11] Norouzi A.M., Siavashi M., Ahmadi R., Tahmasbi M., Experimental study of a parabolic trough solar collector with rotating absorber tube. Renewable Energy, 2021, 168: 734–749.

[12] Qiu Y., Xu Y., Li Q., Wang J., Wang Q., Liu B., Efficiency enhancement of a solar trough collector by combining solar and hot mirrors. Applied Energy, 2021, 299: 117290.

[13] Gong J.H., Wang J., Lund P.D., Hu E.-Y., Xu Z.C., Liu G.P., Li G.S., Improving the performance of a 2-stage large aperture parabolic trough solar concentrator using a secondary reflector designed by adaptive method. Renewable Energy, 2020, 152: 23–33.

[14] Spirkl W.R.H., Muschaweck J., Timinger A., Optimized compact secondary reflectors for parabolic troughs with tubular absorbers. Solar Energy, 1997, 61: 153–158.

[15] Bellos E., Tzivanidis C., Daniil I., Antonopoulos K.A., The impact of internal longitudinal fins in parabolic trough collectors operating with gases. Energy Conversion and Management, 2017, 135: 35–54.

[16] Bellos E., Tzivanidis C., Tsimpoukis D., Enhancing the performance of parabolic trough collectors using nanofluids and turbulators. Renewable and Sustainable Energy Reviews, 2018, 91: 358–375.

[17] Chen X., Xia X.L., Meng X.L., Dong X.H., Thermal performance analysis on a volumetric solar receiver with

double-layer ceramic foam. Energy Conversion and Management, 2015, 97: 282–289.

[18] Shi Y., Sun J., Wei J., Numerical study of new-type receiver with axially-hollow spiral deflector for parabolic trough direct-steam-generation loop of concentrating solar power system. Journal of Thermal Science, 2023: 597–610.

[19] Bellos E., Tzivanidis C., Antonopoulos K.A., Gkinis G., Thermal enhancement of solar parabolic trough collectors by using nanofluids and converging-diverging absorber tube. Renewable Energy, 2016, 94: 213–222.

[20] Javadi F.S., Saidur R., Kamalisarvestani M., Investigating performance improvement of solar collectors by using nanofluids. Renewable and Sustainable Energy Reviews, 2013, 28: 232–245.

[21] Heyhat M.M., Valizade M., Abdolahzade S., Maerefat M., Thermal efficiency enhancement of direct absorption parabolic trough solar collector (DAPTSC) by using nanofluid and metal foam. Energy, 2020, 192: 116662.

[22] He Q., Wang S., Zeng S., Zheng Z., Experimental investigation on photothermal properties of nanofluids for direct absorption solar thermal energy systems. Energy Conversion and Management, 2013, 73: 150–157.

[23] Aggray Mwesigye T.B.-O., Josua P. Meyer, Heat transfer enhancement in a parabolic trough receiver using wall detached twisted tape inserts. in: IMECE2013, San Diego, California, USA, 2013.

[24] Jaramillo O.A., Borunda M., Velazquez-Lucho K.M., Robles M., Parabolic trough solar collector for low enthalpy processes: An analysis of the efficiency enhancement by using twisted tape inserts. Renewable Energy, 2016, 93: 125–141.

[25] Liu P., Lv J., Shan F., Liu Z., Liu W., Effects of rib arrangements on the performance of a parabolic trough receiver with ribbed absorber tube. Applied Thermal Engineering, 2019, 156: 1–13.

[26] Liu P., Zheng N., Liu Z., Liu W., Thermal-hydraulic performance and entropy generation analysis of a parabolic trough receiver with conical strip inserts. Energy Conversion and Management, 2019, 179: 30–45.

[27] Mwesigye A., Bello-Ochende T., Meyer J.P., Heat transfer and thermodynamic performance of a parabolic trough receiver with centrally placed perforated plate inserts. Applied Energy, 2014, 136: 989–1003.

[28] Muñoz J., Abánades A., Analysis of internal helically finned tubes for parabolic trough design by CFD tools. Applied Energy, 2011, 88: 4139–4149.

[29] Bozorg M.V., Hossein Doranehgard M., Hong K., Xiong Q., CFD study of heat transfer and fluid flow in a parabolic trough solar receiver with internal annular porous structure and synthetic oil-Al_2O_3 nanofluid. Renewable Energy, 2020, 145: 2598–2614.

[30] Kumar B.N., Reddy K.S., Numerical investigations on metal foam inserted solar parabolic trough DSG absorber tube for mitigating thermal gradients and enhancing heat transfer. Applied Thermal Engineering, 2020, 178: 115511.

[31] Zhao Z., Bai F., Zhang X., Wang Z., Experimental study of pin finned receiver tubes for a parabolic trough solar air collector. Solar Energy, 2020, 207: 91–102.

[32] Gorjian S., Ebadi H., Calise F., Shukla A., Ingrao C., A review on recent advancements in performance enhancement techniques for low-temperature solar collectors. Energy Conversion and Management, 2020, 222: 113246.

[33] Manuel, D.T.A., Lourdes G.R., Comparison of solar technologies for driving a desalination system by means of an organic Rankine cycle. Desalination, 2007, 216: 276–291.

[34] Qiu Y., Li M.J., He Y.L., Tao W.Q., Thermal performance analysis of a parabolic trough solar collector using supercritical CO_2 as heat transfer fluid under non-uniform solar flux. Applied Thermal Engineering, 2017, 115: 1255–1265.

[35] He Y.L., Xiao J., Cheng Z.D., Tao Y.B., A MCRT and FVM coupled simulation method for energy conversion process in parabolic trough solar collector. Renewable Energy, 2011, 36: 976–985.

[36] Qiu Y., Li M.J., Wang K., Liu Z.B., Xue X.D., Aiming strategy optimization for uniform flux distribution in the receiver of a linear Fresnel solar reflector using a multi-objective genetic algorithm. Applied Energy, 2017, 205: 1394–1407.

[37] Wang Y., Liu Q., Lei J., Jin H., Performance analysis of a parabolic trough solar collector with non-uniform solar flux conditions. International Journal of Heat and Mass Transfer, 2015, 82: 236–249.

[38] Sun J., Liu Q., Hong H., Numerical study of parabolic-trough direct steam generation loop in recirculation mode: Characteristics, performance and general operation strategy. Energy Conversion and Management, 2015, 96: 287–302.

[39] Qiu Y., He Y.L., Wu M., Zheng Z.J., A comprehensive model for optical and thermal characterization of a linear Fresnel solar reflector with a trapezoidal cavity receiver. Renewable Energy, 2016, 97: 129–144.

[40] Hachicha A.A., Rodríguez I., Capdevila R., Oliva A., Heat transfer analysis and numerical simulation of a parabolic trough solar collector. Applied Energy, 2013, 111: 581–592.

[41] Tao W.Q., Numerical Heat Transfer in Chinese, Beijing: Higher Education Press, 2001.

[42] Forristall R., Heat transfer analysis and modeling of a parabolic trough solar receiver implemented in

engineering equation solver. National Renewable Energy Lab, Golden, CO. (United States), 2003.

[43] Kasperski J., Nemś M., Investigation of thermo-hydraulic performance of concentrated solar air-heater with internal multiple-fin array. Applied Thermal Engineering, 2013, 58: 411–419.

[44] Bellos E., Tzivanidis C., Antonopoulos K.A., A detailed working fluid investigation for solar parabolic trough collectors. Applied Thermal Engineering, 2017, 114: 374–386.

[45] Petela R., Exergy of undiluted thermal radiation. Solar Energy, 2003, 74: 469–488.

[46] Bellos E., Tzivanidis C., Enhancing the performance of a parabolic trough collector with combined thermal and optical techniques. Applied Thermal Engineering, 2020,

164: 114496.

[47] Bellos E., Tzivanidis C., Tsimpoukis D., Thermal enhancement of parabolic trough collector with internally finned absorbers. Solar Energy, 2017, 157: 514–531.

[48] Wang K., Zhang Z.D., Li M.J., Min C.H., A coupled optical-thermal-fluid-mechanical analysis of parabolic trough solar receivers using supercritical CO_2 as heat transfer fluid. Applied Thermal Engineering, 2021, 183: 116154.

[49] SurfaceT S.M., Calculation of the concentrated flux density distribution in parabolic trough collectors by a semifinite formulation. Solar Energy, 1986, 37: 335–345.

[50] Dudley VE K.G., Mahoney AR, Test results: SEGS LS-2 solar collector. Sandia National Lab. (SNL-NM), Albuquerque, NM (United States), 1994.